

## Flow visualization over drag reducing dimpled surfaces in turbulent boundary layers using Particle Image Velocimetry

van Campenhout, Olaf; van Nesselrooij, Michiel; Veldhuis, Leo; van Oudheusden, Bas; Schrijer, Ferdinand

**Publication date**

2016

**Document Version**

Accepted author manuscript

**Published in**

Proceedings of the 18th International Symposium on the Application of Laser and Imaging Techniques to Fluid Mechanics

**Citation (APA)**

van Campenhout, O., van Nesselrooij, M., Veldhuis, L., van Oudheusden, B., & Schrijer, F. (2016). Flow visualization over drag reducing dimpled surfaces in turbulent boundary layers using Particle Image Velocimetry. In *Proceedings of the 18th International Symposium on the Application of Laser and Imaging Techniques to Fluid Mechanics: Lisbon, Portugal* Springer.

**Important note**

To cite this publication, please use the final published version (if applicable). Please check the document version above.

**Copyright**

Other than for strictly personal use, it is not permitted to download, forward or distribute the text or part of it, without the consent of the author(s) and/or copyright holder(s), unless the work is under an open content license such as Creative Commons.

**Takedown policy**

Please contact us and provide details if you believe this document breaches copyrights. We will remove access to the work immediately and investigate your claim.

# Flow visualization over drag reducing dimpled surfaces in turbulent boundary layers using Particle Image Velocimetry

O.W.G. (Olaf) van Campenhout<sup>1</sup>, M. (Michiel) van Nesselrooij<sup>1</sup>, L.L.M. (Leo) Veldhuis<sup>2</sup>,  
B.W. (Bas) van Oudheusden<sup>1</sup>, F.F.J. (Ferry) Schrijer<sup>1\*</sup>

1: Dept. of Aerodynamics, Faculty of Aerospace Engineering, Delft University of Technology, the Netherlands

2: Dept. of Flight Performance and Propulsion, Faculty of Aerospace Engineering, Delft University of Technology, the Netherlands

\* Correspondent author: F.F.J.Schrijer@tudelft.nl

**Keywords:** Passive flow control, drag reduction, PIV, turbulent boundary layers

## ABSTRACT

Although various experimental studies have confirmed a potential drag reduction of dimpled surfaces in turbulent boundary layers, the working mechanism behind the effect remains largely unresolved. The goal of this experimental study is to reveal the flow structures that could explain this drag reduction. To this end, flow visualizations over drag reducing dimpled surfaces are performed, using planar and stereoscopic Particle Image Velocimetry (PIV). The PIV measurements show that there is no significant vortex generation in the present dimples, but that instead a *converger-diffuser* type of flow occurs. It can be therefore concluded that it is not the generation of vortices which causes the drag reduction, in contrast to what has been proposed in literature. Based on the present measurements, a new drag reducing mechanism is proposed: the interaction between dimples causes alternating spanwise excitations of the near-wall flow which interacts with the turbulent coherent structures and leads to a reduction of the turbulent drag.

---

## 1. Introduction

Any reduction in vehicle drag or fluid resistance provides a potential of substantial energy savings, with obvious benefits to the economy, environment and overall industrial competitiveness. Over the years, various means of passive flow control have emerged that could potentially reduce drag significantly (Abbas 2013, Gad-el-Hak 2000, Spalart & McLean 2011). Examples are, among others, Natural Laminar Flow (NLF), riblets, large eddy break-up devices (LEBUs), compliant coatings and wavy walls. These techniques have been studied for many years, but they have not found their way into large-scale commercial applications, for example, due to their impact on vehicle design and/or maintainability. A potential alternative passive flow control technique aimed at turbulent drag reduction is the dimpled surface.

Various experimental studies on this technique have been reported, suggesting that dimpled surfaces have a serious potential for turbulent drag reduction. Research by Tay (2015) has shown a drag reduction over dimpled surfaces in a channel flow of up to 3%, while research at Delft University of Technology was reported to achieve a drag reduction of 5-10% for a dimpled plate compared to a flat plate (Veldhuis & Vervoort 2009). Kiknadze (2006) has performed research on dimpled surfaces for many years and presents the formation of vortices in the dimples as the key mechanism for drag reduction. He argues that these vortices could act as fluid-dynamic “ball-bearings” to the flow and/or induce a positive shear force in the regions of reversed flow.

At this stage, however, there is no clear consensus on what constitutes the drag reducing mechanism caused by dimpled surfaces. Therefore, an experimental study was performed with the specific objective to provide a detailed flow visualization, which may lead to a better understanding of the drag reducing mechanism of these dimpled surfaces. Direct force measurements are combined with flow visualizations using Particle Image Velocimetry (PIV). Seven different plates containing various dimple geometries and arrangements have been tested and referenced against a flat plate.

## 2. Methodology

The measured surfaces consist of spherical dimples which are completely described by the following parameters: diameter ( $D$ ), depth ( $d$ ), edge curvature radius ( $r$ ), centre-to-centre streamwise dimple spacing ( $L_x$ ) and spanwise dimple spacing ( $L_z$ ). All lengths are non-dimensionalized by the dimple diameter ( $D$ ). Furthermore, the dimple coverage ratio can be defined as the total surface of all dimples with respect to the total surface of the plate. The impact of the relative boundary layer thickness ( $\delta/d$ ) was investigated by varying dimple depths and by measuring all dimples for two different boundary layer thicknesses (approximately 15 mm and 30 mm, respectively). Both staggered and aligned patterns, as defined in Fig. 1, were investigated. Tab. 1 gives an overview of the tested dimpled surfaces and Fig. 2 presents the cross-sectional geometry of a single dimple.

**Tab. 1** Overview of tested dimple design parameters.

Configuration	$D$ (mm)	$d/D$	$L_x/D$	$L_z/D$	Coverage	$\delta/d$ (thin)	$\delta/d$ (thick)	Pattern
A	20	2.5%	2.859	1.650	33.3%	30	60	Staggered
B	20	2.5%	1.650	2.859	33.3%	30	60	Aligned
C	20	2.5%	1.739	1.003	90%	30	60	Staggered
D	60	2.5%	1.739	1.003	90%	10	20	Staggered
E	20	5%	2.859	1.650	33.3%	15	30	Staggered
F	20	5%	1.739	1.003	90%	15	30	Staggered
G	60	5%	1.739	1.003	90%	5	10	Staggered

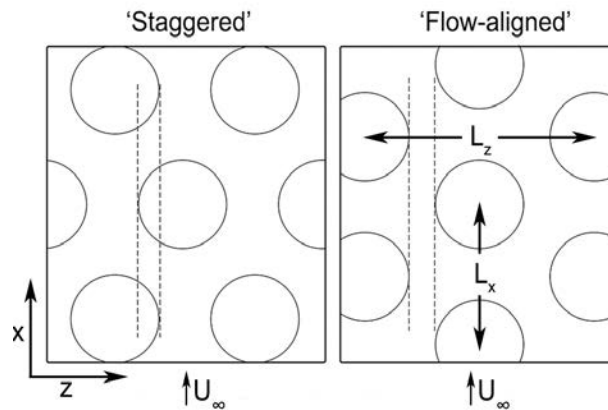


**Fig. 1** Definition of streamwise and spanwise dimple spacing ( $L_x$ ,  $L_z$ ) and the difference between a staggered and flow-aligned pattern. The mean flow  $U_\infty$  is in x-direction.

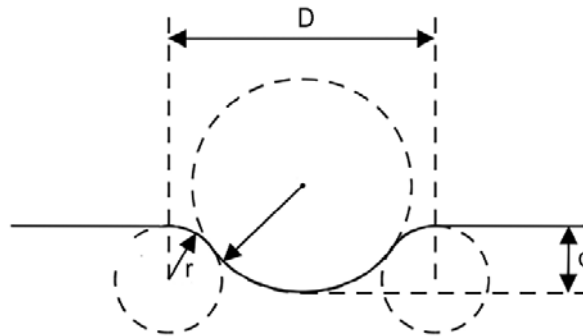


**Fig. 2** Cross-sectional geometry of a rounded spherical dimple. Depth is exaggerated for clarity.

The plates were tested in a low-speed wind tunnel, which has a cross section of 40x40 cm, for flow speeds up to 30 m/s. The test section has a transparent wall and is thereby well-suited for PIV measurements. A freely suspended pendulum setup was used to perform the direct force measurements, of which a schematic overview can be found in Fig. 3.

The test plates (4) are manufactured from Polyoximethylene (POM) plastic and have a size of 669x351 mm. The test plates are mounted in an aluminium frame (2) which is suspended by metal wires (3) just above the wind tunnel floor (7). A metal rod at the bottom of the test frame is connected to the force sensor (6), a KD40S-2N by ME-Meßsysteme GmbH. A flow deflector (1) is placed in front of the leading edge of the aluminium test frame and is equipped with carborundum roughness elements to trip the boundary layer. A fine mesh cylinder with a diameter of 6 mm could be placed approximately 60 cm upstream of the test plate, increasing the boundary layer thickness above the test plate from  $\delta \approx 15$  mm (thin boundary layer) to  $\delta \approx 30$  mm (thick boundary layer). At the trailing edge, a horizontal element (5) guides the flow towards the exit of the tunnel.

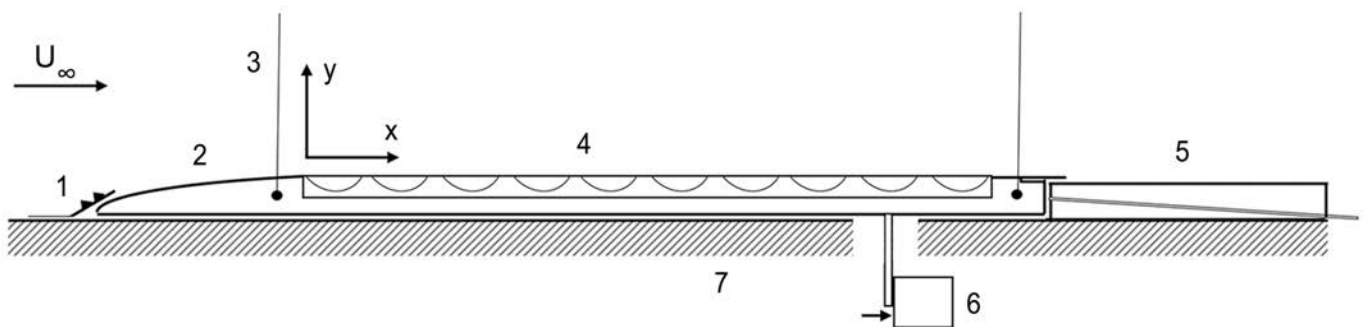


**Fig. 3** Schematic side view of the drag measurement setup. 1) deflector with carborundum roughness elements, 2) suspended test frame, 3) pendulum cable, 4) test plate, 5) rear flow guide, 6) force sensor, 7) wind tunnel floor.

Of the tested dimpled surfaces, the A-configuration was the only plate for which a drag reduction was found within the tested Reynolds regime (approximately 10,000 - 40,000, based on dimple diameter and the free stream flow velocity). For the B, C, D and E-configuration plates, a drag increase was found of up to 6%. While the G and F-configurations have shown drag increases of up to 20%. The A-configuration plate, on the other hand, repeatedly delivered a drag reduction of up to 4%. The measured drag of the A-configuration plate relative to flat plate drag is plotted against Reynolds number (based on dimple diameter) in Fig. 4. A drag reduction was found for both the thin and the thick boundary layer. Furthermore, the measured drag reduction increases with increasing Reynolds number. This Reynolds number dependency of the drag reduction makes investigations of the higher Reynolds number regime interesting for future studies. Interestingly, when rotating the A-configuration dimples by 90 degrees such that it becomes a flow-aligned pattern (B-configuration), no drag reduction is observed. This suggests an interaction between the dimple-induced flows.

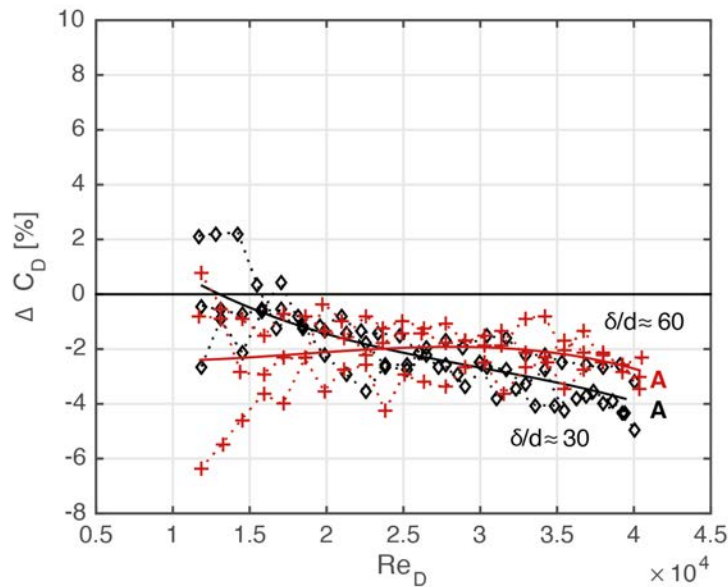


**Fig. 4** Drag performance of the A-configuration plate relative to a flat plate for the thin (black) and thick (red) boundary layer. Data points indicate measurement points and solid lines indicate the mean.  $Re_D$  is based on a dimple diameter of 20 mm and freestream velocity as  $Re_D = U_\infty D/\nu$ .

### 3. PIV setup

To obtain a better understanding of the drag reduction mechanism of dimples, high-resolution and non-intrusive flow field measurements of the local 3D flow structure and near-wall instantaneous velocity and turbulence footprints are required. To this end, the flow fields over the dimpled surfaces were measured using two visualization configurations:

- The first provides a planar panoramic flow field representation, which captures the full boundary layer and spans multiple dimples in order to document their influence on boundary layer parameters. This is achieved by using two cameras operating in 2C mode, as depicted in Fig. 5.a.
- The second configuration aims to provide a 3D representation of the flow in a single dimple (20 mm diameter) in order to reveal the flow structure inside the dimple. The available knowledge of 6 possible dimple flow structures (Kovalenko 2010, Tay 2014) indicates that the measured flow structure may be quasi-steady or oscillating between two orientations. Thus, stereoscopic PIV measurements in several planes across the dimple, as depicted in Fig. 5.b, will suffice to reconstruct the full 3D mean flow field.

Given its drag performance, the focus of the flow visualization lies on the A-configuration plate.

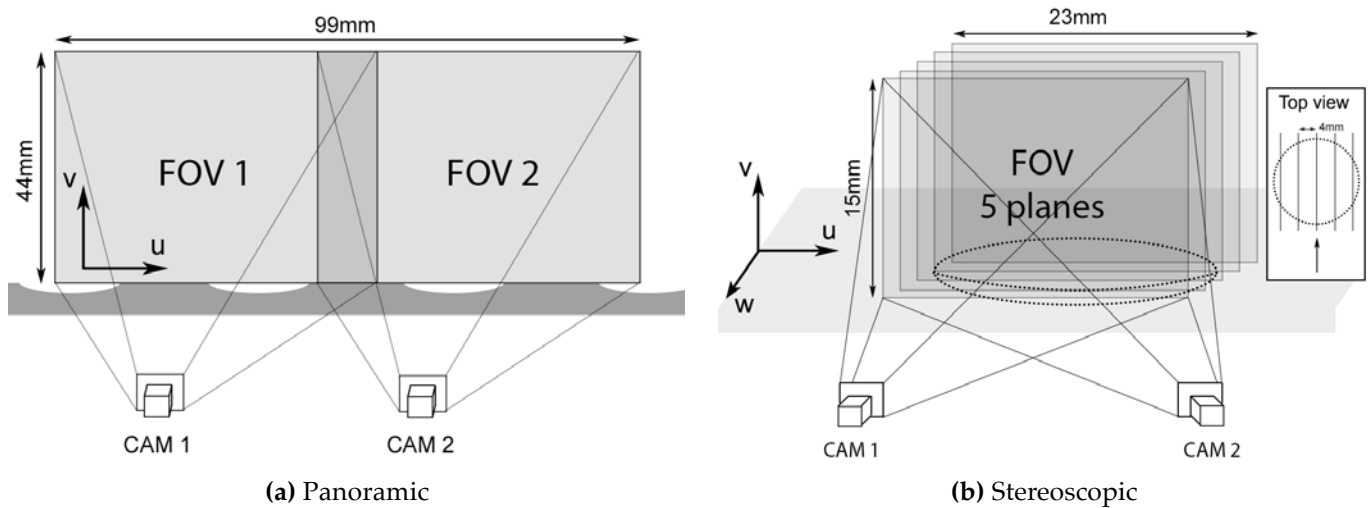


Fig. 5 PIV configurations showing the locations of the field of view (FOV) w.r.t. the dimpled surfaces.

To perform the PIV measurements, a laser sheet is directed into the test section from the open end of the wind tunnel. The laser sheet is oriented vertically and parallel with the free stream flow direction and has a width of approximately 2 mm at the measurement location. The panoramic setup as well as the stereoscopic setup are used to investigate the flow at freestream velocities of 15 m/s and 30 m/s. The fields of view for the panoramic setup have an overlap of approximately 15% and are aligned horizontally with the test plate to minimize the laser reflections in the images. This increases the reliability of the near wall data, albeit obstructing optical access of the cameras inside the dimples (as depicted in Fig 5.a).

For the stereoscopic investigation, the angle enclosed by the cameras is 45 degrees, providing a good balance between in- and out-of-plane velocity accuracy (Prasad 2000). The cameras are fitted with Scheimpflug adapters, which position the lenses at an angle of approximately 10 degrees relative to the camera sensors. As can be seen from Fig. 5.b, the dimple is visualized in five planes to allow the reconstruction of the 3D flow field statistics. This is achieved by traversing the laser optics and cameras across a rail simultaneously. The planes are aligned with the freestream velocity and they are located at 10, 30, 50, 70 and 90% of the dimple diameter. Details on total field of view (FOV), spatial resolution, vector pitch and pulse separation time are given in Tab. 2.

Tab. 2 Summary of PIV settings.

PIV setup	Total FOV	px/mm	Vector pitch	$\Delta t$ (15 m/s)	$\Delta t$ (30 m/s)
Panorama	99x44 mm	24	0.34 mm	25 $\mu$ s	13 $\mu$ s
Stereo	23x15 mm	65	0.13 mm	12 $\mu$ s	6 $\mu$ s

The recording equipment consists of two PCO CCD SensiCam QE cameras with cooled 1376x1040 px sensors fitted with a Scheimpflug adapter and AF Micro Nikkor 105 mm lenses. The aperture has been set to  $f/11$  for all the measurements. Illumination is provided by a double-pulsed ND:Yag Big Sky Laser by Quantel, type CFR PIV200. The seeding is achieved using a Safex® fog generator. Each measurement consists of 3 sets of each 100 images (thus  $N = 300$ ), which are acquired at 30 Hz. This acquisition rate allows for statistical characterization of the flow, however it is insufficient to capture the time-resolved flow development. The Lavision DAVIS 8.0 software is used for camera and laser control and PIV processing.

The PIV processing is performed using an interrogation window of 96x96 px and a 50% overlap in the first iteration followed by three iterations based on 4:1 elliptical interrogation windows (equivalent window size of 32x32 px) with 75% overlap. The final vector spacing is 0.34 mm for the panoramic results and 0.13 mm for the stereoscopic results. The instantaneous in-plane velocity vector errors are estimated to be around 0.8% of the freestream velocity, based on 0.1 pixel correlation noise (Raffel 1998) and a 12 pixel average displacement in the freestream. The instantaneous error of the out-of-plane velocity field is estimated using equation 1 after Prasad (2000), where  $\theta$  is the off-axis half-angle of the lens planes.

$$\frac{\sigma_{\Delta z}}{\sigma_{\Delta x}} = \frac{2d_0}{s} = \frac{1}{\tan \theta} \quad (1)$$

The uncertainty in the mean and RMS vector field as obtained from  $N$  flow fields is determined by equation 2 and equation 3 respectively (Benedict & Gould 1996).

$$\epsilon_{\bar{u}} = \frac{u'}{\sqrt{N}} \quad (2)$$

$$\epsilon_{u'} = \frac{u'}{\sqrt{2N}} \quad (3)$$

For  $U_\infty = 30$  m/s, typical maximum values for  $u'$ ,  $v'$  and  $w'$  are 3.8, 1.2 and 1.9 m/s. The panoramic results capture less of these near wall fluctuations. The results for the PIV uncertainty calculations are summarized in Tab. 3.

**Tab. 3** PIV velocity error estimates at  $U_\infty = 30$  m/s [expressed as % $U_\infty$ ].

	$\epsilon_u$	$\epsilon_v$	$\epsilon_w$	$\epsilon_{\bar{u}}$	$\epsilon_{\bar{v}}$	$\epsilon_{\bar{w}}$	$\epsilon_{u'}$	$\epsilon_{v'}$	$\epsilon_{w'}$
Panoramic	0.83	0.83	-	0.41	0.22	-	0.29	0.15	-
Stereoscopic	0.83	0.83	0.95	0.73	0.23	0.37	0.52	0.16	0.26

## 4. PIV Results

### 4.1 Boundary Layer Properties

Using the results of the panoramic PIV data, first the boundary layer on the flat plate is inspected. Fig. 6 shows both the thin ( $\delta \approx 15$  mm) as well as the thick ( $\delta \approx 30$  mm) boundary layer velocity profile in comparison to Spalding's Law of the Wall. Furthermore, the turbulence intensity profiles of the flat plate boundary layers are presented in Fig. 7. The maximum values for  $u'$  are achieved close to the wall and have a value of 3.7 m/s and 3.1 m/s for the thin and thick boundary layer respectively. For  $v'$  the maxima are 0.46 m/s at  $y/\delta = 0.22$  for the thin boundary layer and 0.64 m/s and  $y/\delta = 0.37$  for the thick boundary layer. Details on momentum thickness ( $\theta$ ), shape factor ( $H$ ), friction velocity ( $u^* = \sqrt{\tau_w/\rho}$ ) and skin friction ( $C_f$ ) are given in Tab. 4.

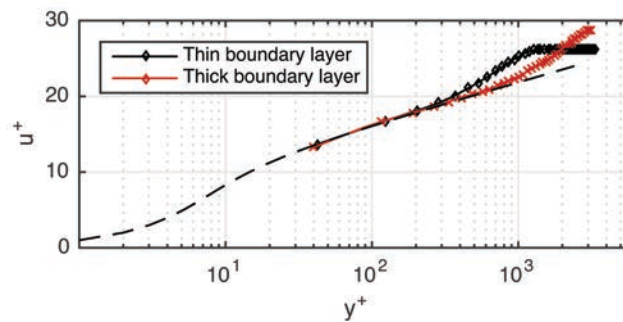


**Fig. 6** Mean velocity profiles at the centre of the flat test plate and at  $Re_D \approx 40,000$ . Every third data point is shown. Obtained using the panoramic PIV data. Dashed line indicates Spalding's Law of the Wall.

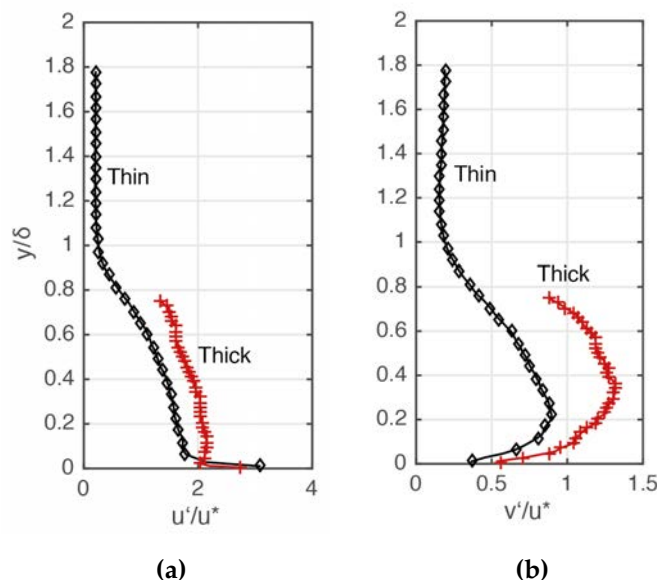


**Fig. 7** Turbulence intensity profiles at the centre of the flat test plate and at  $Re_D \approx 40,000$ . Every third data point is shown. Obtained using the panoramic PIV data.

**Tab. 4** Boundary layer characteristics as obtained using the panoramic PIV data at the centre of the flat test plate at  $Re_D \approx 40,000$ .

Boundary Layer	$\theta$	$H$	$u^*$	$C_f$
Thin	1.84	1.48	1.21	0.0033
Thick	1.72	1.43	1.11	0.0027

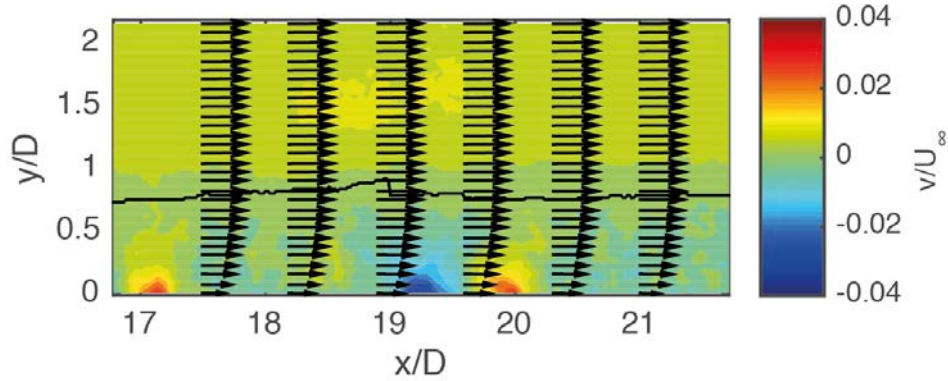


**Fig. 8** Panoramic PIV results of plate A at  $Re_D \approx 40,000$  (thin boundary layer). Shows contours of  $v$ , local  $\delta$  (solid black line) and selected velocity vectors.  $x/D = 0$  defined at the start of the test plate.

Fig. 8 shows a typical panoramic PIV measurement result for the A-configuration dimpled surface. Using the panoramic PIV data, the development of boundary layer thickness ( $\delta$ ), displacement thickness ( $\delta^*$ ), momentum thickness ( $\theta$ ) and shape factor ( $H$ ) over the A-configuration dimples has been analysed. Interestingly, the averaged boundary layer properties were not significantly affected by the dimpled surface with respect to the flat plate. However, inspecting the boundary layer locally, it is observed that as the flow moves from one dimple to another over the intermediate flat surface, consistently an initial deceleration is observed which is followed by an acceleration in the near-wall region. This is also observed from the shape factor development, which can be seen in Fig. 9. The increase in  $H$  indicates an increasing pressure and hence a deceleration of the flow, followed by acceleration towards the next dimple.

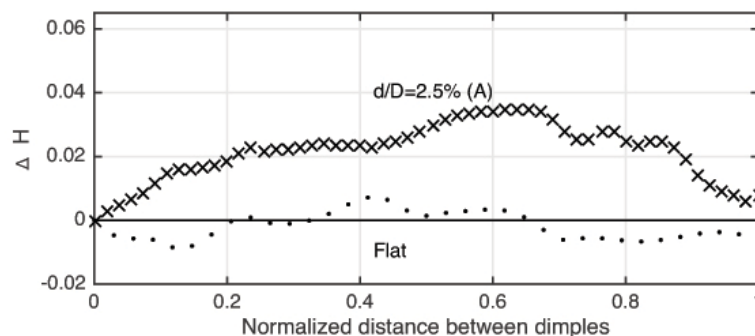


**Fig. 9** Development of the shape factor over the flat region between two dimples (dimple exit at  $x = 0$ , to dimple entry at  $x = 1$ ) at  $Re_D \approx 40,000$  (thin boundary layer). Obtained from panoramic data over plate A. At  $x = 0$ , the shape factors are 1.51 and 1.49 for the flat and dimpled case respectively.

## 4.2 Flow structures

From the stereoscopic PIV data, it can be observed that the flow is decelerated inside and above the dimple. Nevertheless, there is no separation or flow reversal observed in the drag-reducing dimples in any of the instantaneous velocity fields. This is therefore also true for the mean flow presented in Fig. 10b, which can be compared to the mean flow over the flat plate shown in Fig. 10a. Since the vector closest to the surface lies rather close to the wall (0.13 mm which corresponds to  $0.0065D$  or  $0.009\delta$ ), any separation even closer to the surface is very limited at most.

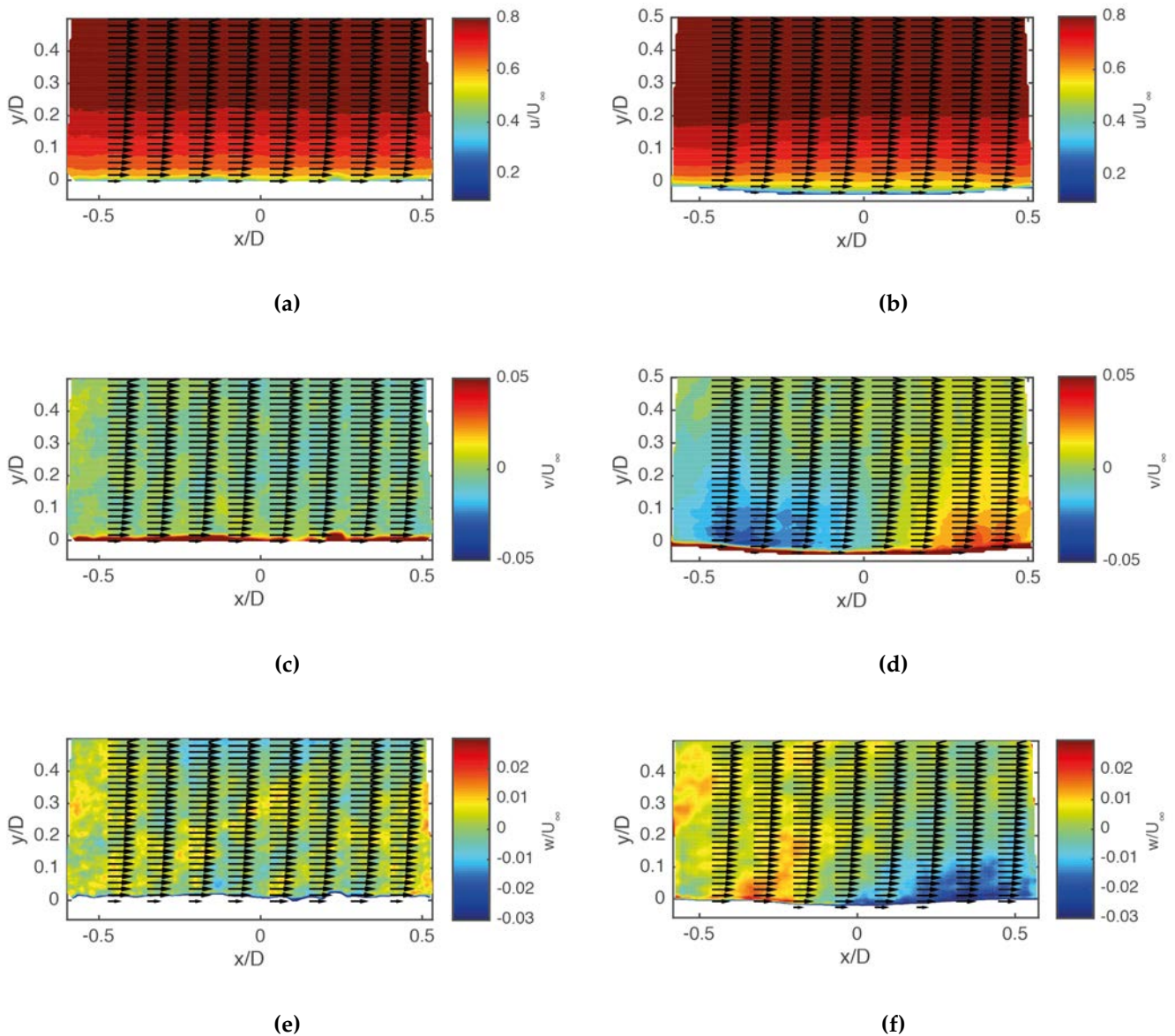


**Fig. 10** Mean velocity components in the plane along the centreline of flat plate (left) and A-configuration dimple (right). Obtained from stereoscopic PIV data at  $Re_D \approx 40,000$  (thin boundary layer).

Fig. 11 shows the top view of the mean flow topology as reconstructed from the five stereoscopic measurement planes at approximately 1 mm above the surface. The results are presented for dimple configuration A, B, C and E at a Reynolds number (based on dimple diameter) of 40,000. The streaklines and the contours of the spanwise velocity reveal that a *converger-diffuser* type of flow is present in all tested dimples, which is in agreement with the prediction by Tay (2014). The structure of the flow is not substantially different for any of the tested dimples, nevertheless, a drag reduction was only observed in the A-configuration dimples. The spanwise velocity component is approximately on the order of 2-3% of the freestream velocity for all geometries and extends up to 0.1-0.2D above the surface.

The flow deceleration inside the dimple is confirmed by Fig. 11 as well as the acceleration at the entry and exit of the dimple. The high-velocity region near the edges of the dimple spans a larger region in the B-configuration compared to the A, C and E configurations. Furthermore, in the high coverage ratio pattern (C), the high-velocity region is most pronounced at the boundaries with the neighbouring dimples. Changing the Reynolds number from 40,000 to 20,000 (not shown in this manuscript) does not alter the flow structures as observed from the PIV data. Apparently, the increasing drag reduction with Reynolds number is not related to a change in the flow topology. Also when increasing the boundary layer thickness (not shown in this manuscript) the flow topology stays the same.

To get a better understanding of the interaction between the dimples, an additional surface oil flow visualization was performed. Fig. 12.a shows the results for the drag-reducing dimples (A-configuration), while Fig. 12.b shows the results for the same dimples in the aligned configuration (B-configuration). The oil flow patterns reveal an interesting difference: in Fig. 12.a, longitudinal structures in the oil flow appear that are seen to jump from a dimple to the staggered dimple creating a somewhat oscillatory path, similar to what is sketched in the insert in Fig. 11 (top right). In Fig. 12.b, on the other hand, these paths appear to move from a dimple to the next downstream dimple, with less oscillatory behaviour.

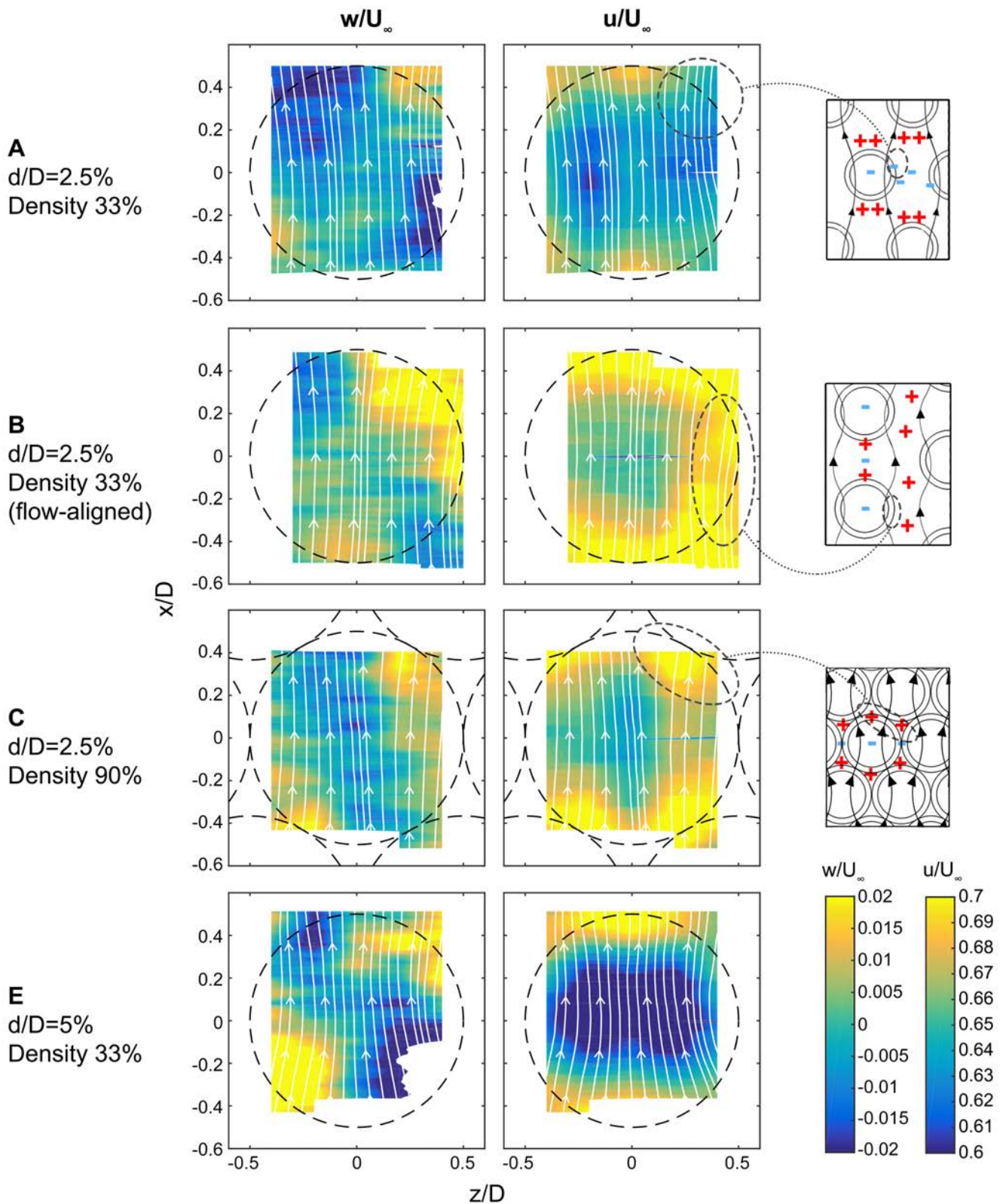
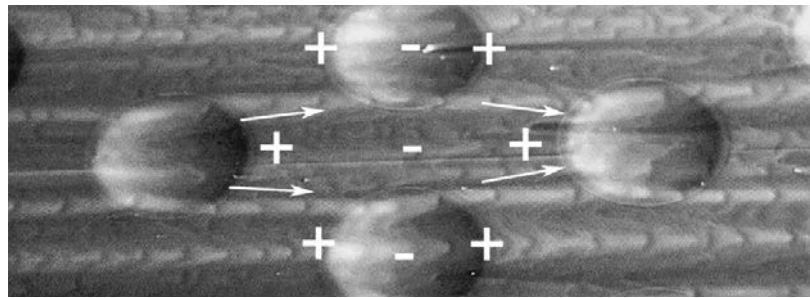
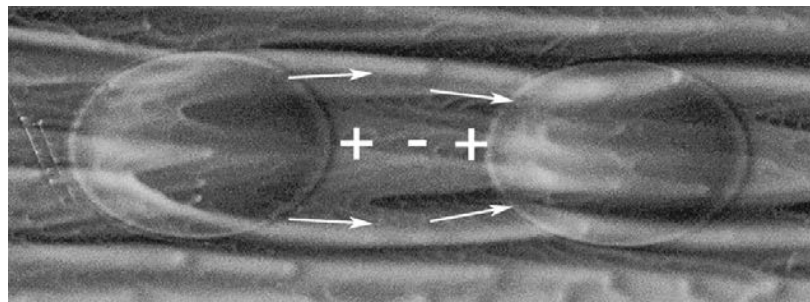


**Fig. 11** Top view of the flow structures reconstructed from 5 stereoscopic PIV planes at 1 mm above the local surface.

Left:  $u/U_\infty$  contours, right:  $w/U_\infty$  contours. Thin boundary layer case at  $Re_D \approx 40,000$ . The  $w$ -component in the streaklines is amplified 5 times for clarity. Symbols in the schematic drawings (right) indicate areas where high (+) and low (-) velocity is expected.



(a)

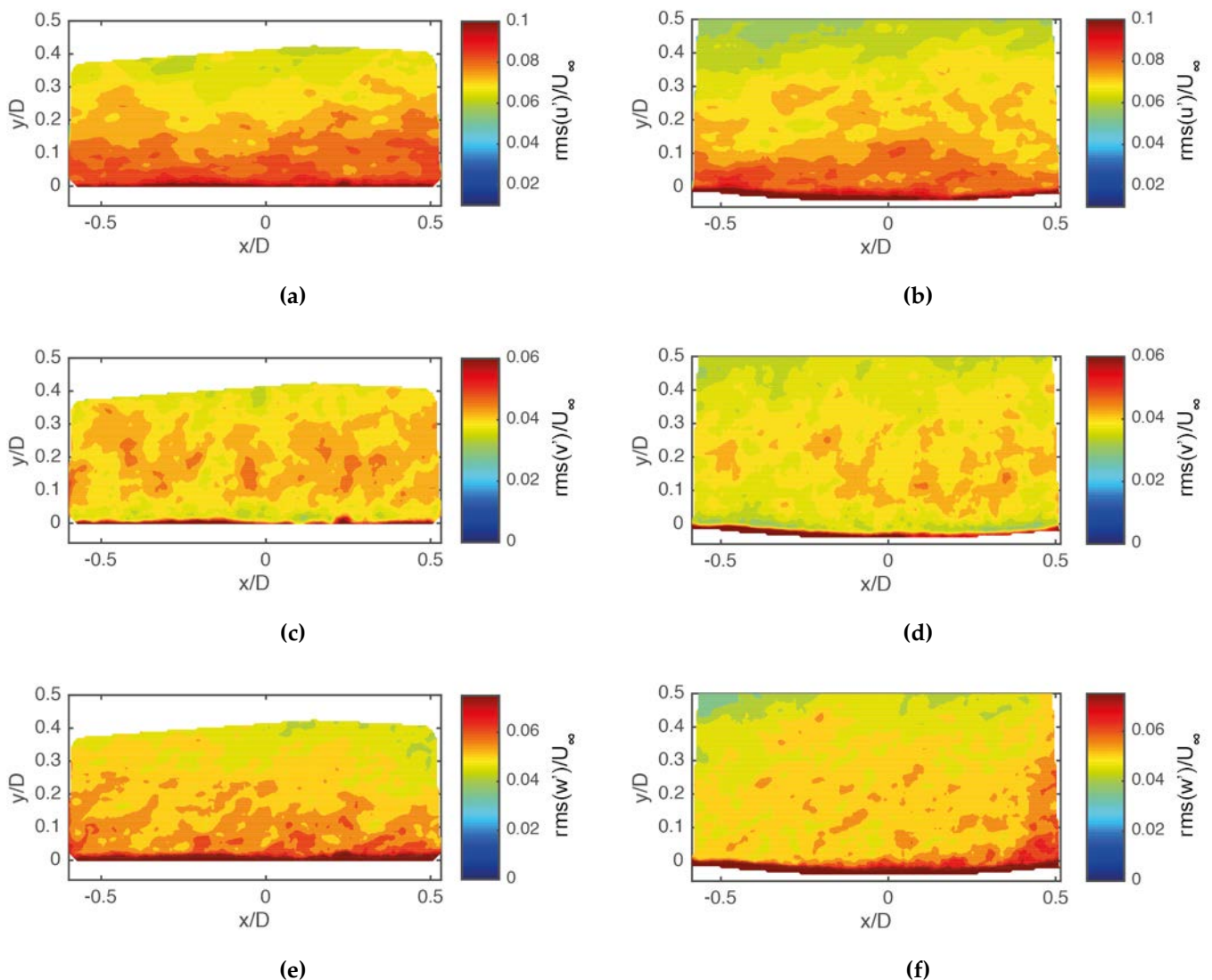


(b)

**Fig. 12** Photograph of fluorescent oil flow visualization at  $Re_D \approx 40,000$  (thin boundary layer) over dimpled surfaces with  $d/D = 2.5\%$  in A-configuration staggered (a) and B-configuration flow-aligned (b). Symbols indicate areas where high (+) and low (-) velocity are expected. Dimples are shown slightly elliptical due to the oblique viewing angle.

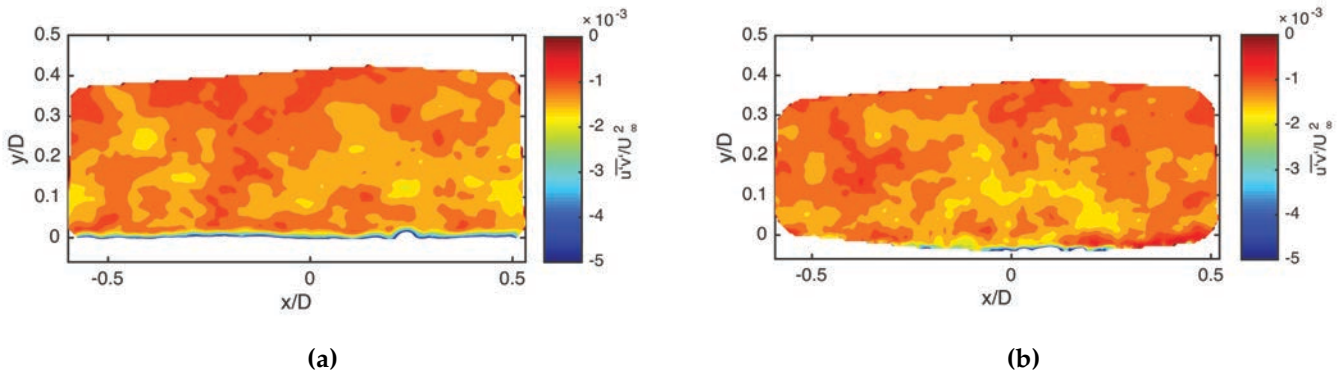
### 4.3 Effect on turbulence

Fig. 13 presents the Root Mean Square (RMS) of the velocity fluctuations ( $u'$ ,  $v'$  and  $w'$ ) of the flow through the centre of the A-configuration dimple as well as over the flat plate. The observed differences between the flat plate and the A-configuration dimple are small. However, the fluctuations in  $u'$  and  $v'$  are somewhat reduced around the entry and exit locations of the dimple compared to the flat plate. It appears that fluctuations in the spanwise direction are slightly damped by the presence of the dimple, although these differences are close to the uncertainties presented in Tab. 3. The increased value of  $w'$  at the dimple exit may be caused by particles at the edge of the FOV which are out of focus. Outliers ( $>3\sigma$ ) are filtered in the calculation of the RMS values.



**Fig. 13** RMS of velocity fluctuations along centreline of A-configuration dimple (right) and flat plate (left). Obtained from stereoscopic PIV data at  $Re_D \approx 40,000$  (thin boundary layer).

Using the stereoscopic PIV results, the Reynolds Stress footprint is calculated through the centreline of the A-configuration dimple as well as the flat plate, as depicted in Fig. 14. The difference between the Reynolds stress footprint of the A-configuration dimples and the flat plate is seen to be small.



**Fig. 14** Average Reynolds stress along the centreline of A-configuration dimple (right) and flat plate (left). Obtained from stereoscopic PIV data and at  $Re_D \approx 40,000$  (thin boundary layer).

When inspecting the Reynolds stress profile, as presented in Fig. 15, the average value of the Reynolds stress of the data point closest to the surface is seen to be lower above the dimple compared to the flat plate, and similar elsewhere. However, it must be noted that a significant difference is only measured for a single data point, and that the rest of the flow field is not fully converged using the available 300 image pairs, as seen in Fig. 14 and 15, and in the range of the uncertainties given in Tab. 3.

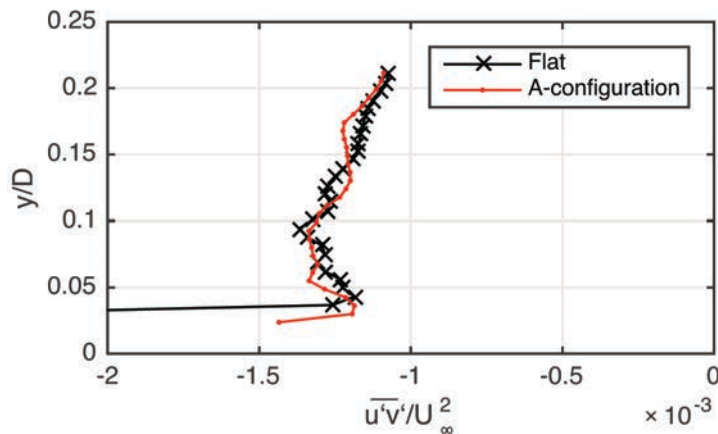


**Fig. 15** Average Reynolds stress profile for the flat and A-configuration dimple over the domain shown in Fig. 14, where  $y = 0$  is taken at the local surface. Every second data point is shown.

The instantaneous flow through a dimple is presented in Fig. 16. It can be noted that the PIV measurements provide the necessary spatial resolution to capture the turbulent coherent structures in the boundary layer. Packets of vortices can be identified as well as sweep and ejection events.

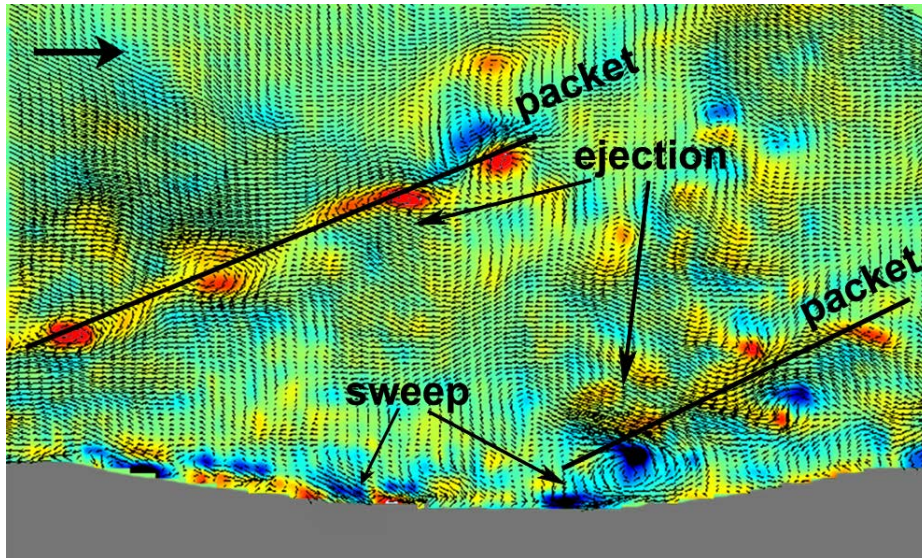


**Fig. 16** Instantaneous vorticity  $\omega$  (red is clockwise and blue is counter-clockwise) throughout dimple cross section ( $d/D = 5\%$ ). Stereoscopic PIV of plate E. Packets of hairpin vortices and typical ejection and sweep events are clearly captured in the data. Mean flow subtracted.

Fig. 17 presents a quadrant analysis from the stereoscopic PIV data, based on all 300 image pairs. A row of ten vectors is analysed at the centre of the dimple at a height of  $0.1\delta$  and  $0.5\delta$  ( $0.075D$  and  $0.375D$  respectively), resulting in 3000 data points. The scatter plots are all typical of a turbulent boundary layer, showing emphasis on sweep (Q4) and ejection (Q2) events. At  $y/\delta = 0.5$  the occurrence of sweep and ejection events is reduced from 66.9% to 65.2% by the dimple, as presented in Tab. 5. This observation may point to turbulence reduction as the mechanism associated with drag-reducing dimples. At  $y/\delta = 0.1$  the occurrences of sweep and ejection events differ little: 64.8% and 64.7% for the flat and A-configuration respectively. It must be considered that this is within statistical uncertainty.

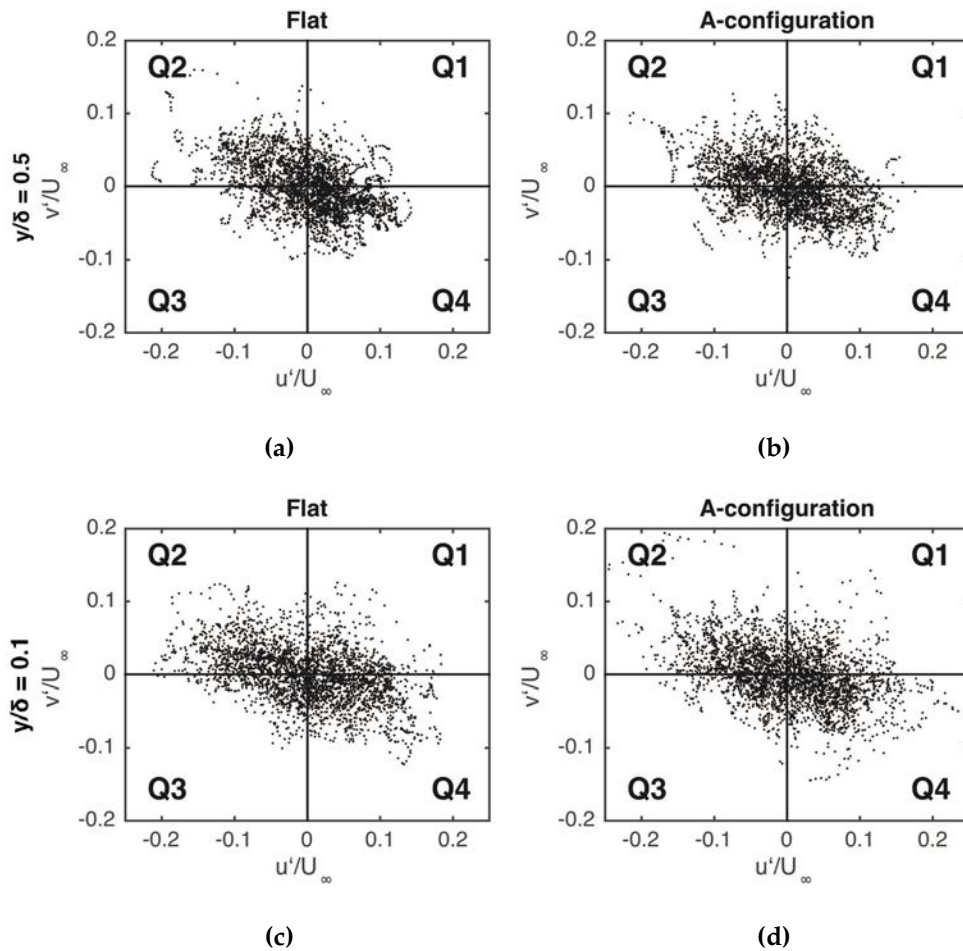


**Fig. 17** Quadrant analysis of the flow above the centre of an A-configuration dimple (right) and a flat plate (left) as measured with stereoscopic PIV at  $y/\delta = 0.5$  (upper) and  $y/\delta = 0.1$  (lower) where  $Re_D \approx 40,000$  (thin boundary layer).

**Tab. 5** Overview of quantitative quadrant analysis of the boundary layer above a flat plate and A-configuration dimple, as measured with stereoscopic PIV at  $y/\delta = 0.1$  and  $y/\delta = 0.5$  where  $Re_D \approx 40,000$  (thin boundary layer).

	Occurrences Q2 and Q4	
	= 0.1	= 0.5
Flat	64.80%	66.93%
A-configuration	64.70%	65.23%

## 5. Discussion on the drag reducing mechanism

The flow visualizations as presented in this manuscript show that for all tested geometries and velocities, a *converger-diffuser* type of flow occurs. In the absence of any sharp edges in the geometries, there is no separation nor are there any other complex flow structures to be observed inside the dimples. Therefore, it is unlikely that the formation of vortices in the dimples is the key mechanism for drag reduction, as argued by Kiknadze (2006). Instead, the measurements lead to the suggestion that the drag reduction effect is related to the interaction of the flow structures induced by the individual dimples. This is suggested due to the combination of:

- 1) A confirmation of turbulent drag reduction by staggered patterns of shallow dimples (A-configuration) and the absence of the phenomenon for an aligned pattern of the same dimples (B-configuration).
- 2) The identification of the *converger-diffuser* flow type for these dimples.

Specifically, based on the deduced surface flow pattern, as indicated by the PIV measurements and supported by the surface oil flow visualizations, the shallow dimples in a staggered pattern induce alternating spanwise excitations of the near-wall flow. Such a pattern bears resemblance to an alternating spanwise shear layer which develops in proximity of an oscillating the wall in spanwise direction, thereby creating a Stokes layer.

These spanwise wall oscillations have been proven to be highly effective at reducing the intensity of hairpin vortices and thereby reducing the turbulent drag. Choi & Clayton (2001) have reported drag reductions of up to 45% achieved by means of spanwise wall oscillations. Yakeno (2014) describes how spanwise oscillating walls induce a near-wall shear layer which reduces the strength of the legs of the hairpin vortices. By increasing the Reynolds number, the spanwise shear component as well as the oscillation frequency which is felt by passing vortices is enhanced, which could be a possible explanation of the Reynolds dependency of the direct force results which are presented in this manuscript.

All in all, it seems that the alternating spanwise excitations of the near-wall flow induced by shallow dimples in a staggered pattern show a strong analogy with spanwise wall oscillations which are expected to reduce the intensity of hairpin vortices. In an independent research, Tay (2015) has recently postulated a similar hypothesis to explain the drag reducing dimple effect.

Based on the results from this study, it is concluded that to better understand the drag reduction mechanism, the surface friction distribution of the drag reducing dimpled surface should be studied in combination with the coherent structures in the turbulent boundary layer. This could reveal whether the skin friction reduction is caused by the mean flow structures or by the interaction with the boundary layer turbulence.

## 6. Conclusion

The objective of this study has been to provide a detailed flow visualization that may lead to a better understanding of the drag reducing mechanism of dimpled surfaces. Using direct force measurements, a drag reduction has been confirmed for a staggered pattern of dimples (A-configuration) and a detailed flow visualization has been performed using planar (panoramic) and stereoscopic PIV. The PIV measurements show that the responsible flow structure has a *converger-diffuser* topology. Furthermore, no flow separation has been observed at any point. The induced spanwise velocity extends to approximately  $0.1-0.2D$  above the surface and reaches a magnitude of approximately 2% of the free stream velocity. There is a high velocity region at the entry and exit of the dimple, while a low velocity region is present inside the dimple.

Based on the PIV measurements and surface oil flow visualizations, it has been proposed that the interaction between dimples creates a pattern of alternating spanwise velocity over the surface. It is also proposed that this pattern reduces the strength of the hairpin vortices and that the interaction with the coherent structures in the turbulent boundary layer reduces the skin friction in analogy with drag reduction by spanwise wall oscillations.

Dimples potentially have substantial advantages over other means of passive flow control for drag reduction: they are very shallow and thereby do not require complicated cleaning or maintenance procedures, also they are not prone to wear such as riblets. Furthermore, they can easily be (retro)fitted on skin panels and do not pose substantial design restrictions, as they are very shallow. On the other hand, the direct force measurements have shown that not all dimples are capable of achieving a drag reduction and the drag reduction mechanism is sensitive to dimple design, flow direction and flow conditions. Further research is thereby deemed necessary to understand these sensitivities and to investigate the proposed drag reducing mechanism based on alternating spanwise excitations of the near-wall flow.

## References

- Abbas A, De Vicente J, Valero, E (2013) Aerodynamic technologies to improve aircraft performance. *Aerosp Sci Technol* 28(1):100-132
- Benedict LH, Gould RD (1996) Towards better uncertainty estimates for turbulence statistics. *Exp Fluids* 22(2):129-136, DOI 10.1007/s003480050030
- Choi KS, Clayton BR (2001) The mechanism of turbulent drag reduction with wall oscillation. *Int J Heat Fluid Fl* 22(1):1-9
- Gad-el-Hak, M (2000) *Flow Control: Passive, active and reactive flow management*. Cambridge University Press, New York
- Kiknadze GI, Gachechiladze IA, Oleinikov VG, Alekseev VV (2006) Mechanisms of the self-organization of tornado-like jets owing past three-dimensional concave reliefs. *Heat Transf Res* 37(6):467-494
- Kovalenko GV, Terekhov VI, Khalatov AA (2010) Flow regimes in a single dimple on the channel surface. *J Appl Mech Tech Phy* 51(6):839-848
- Prasad AK (2000) Stereoscopic particle image velocimetry. *Exp Fluids* 29:103-116
- Raffel M, Willert C, Kompenhans J (1998) *Particle Image Velocimetry: A Practical Guide*. Springer, Berlin
- Spalart PR, McLean JD (2011) Drag reduction: enticing turbulence, and then an industry. *Philos T Roy Soc A* 369(1940):1556-1569
- Tay CM, Chew YT, Khoo BC, Zhao JB (2014) Development of flow structures over dimples. *Exp Therm Fluid Sci* 52:278-287, DOI 10.1016/j.expthermusci.2013.10.001
- Tay CMJ, Khoo BC, Chew YT (2015) Mechanics of drag reduction by shallow dimples in channel flow. *Phys Fluids* 27(3):035109, DOI 10.1063/1.4915069

Veldhuis L, Vervoort E (2009) Drag effect of a dented surface in a turbulent flow. In: 27th AIAA Applied Aerodynamics Conference, DOI <http://dx.doi.org/10.2514/6.2009-3950>

Yakeno A, Hasegawa Y, Kasagi N (2014) Modification of quasi-streamwise vortical structure in a drag-reduced turbulent channel flow with spanwise wall oscillation. *Phys Fluids* 26(8):85-109, DOI [10.1063/1.4893903](https://doi.org/10.1063/1.4893903)